

Article

Effect of High-Intensity Microwave Treatment on Structural and Chemical Characteristics of Chinese Fir

Xiaomei Liao ^{1,2,3}, Xuan Fang ¹, Xin Gao ¹, Songlin Yi ² and Yongdong Zhou ^{1,*}

¹ Research Institute of Wood Industry, Chinese Academy of Forestry, Beijing 100091, China; liaoxiaomei@njfu.edu.cn (X.L.); fangxuan@caf.ac.cn (X.F.); gaoxin@caf.ac.cn (X.G.)

² College Materials Science and Technology, Beijing Forestry University, Beijing 100083, China; ysonglin@bjfu.edu.cn

³ College Furnishings and Industrial Design, Nanjing Forestry University, Nanjing 210037, China

* Correspondence: zhouyd@caf.ac.cn

Abstract: High-intensity microwave (HIMW) treatment is a time-saving and environmentally friendly method widely applied in the wood processing industry. It enhances wood permeability, making it suitable for drying and impregnation modification. This study aimed to investigate the effects of HIMW on macroscopic and microscopic cracks, tracheid cell wall damage, and the chemical structure of Chinese fir [*Cunninghamia lanceolata* (Lamb.) Hook] wood. Through the use of a camera, optical microscope, scanning electron microscope, transmission electron microscope, Fourier-transform infrared spectroscopy, and X-ray diffraction, the morphology of cracks, cell wall damage, the chemical composition of the cell wall, and the crystalline structure of cellulose treated with HIMW were examined and analyzed. The results revealed that the initial moisture content (MC) and microwave energy density (MWED) significantly influenced the crack characteristics and cell wall structure and slightly influenced the chemical composition and crystalline structure of cellulose of the Chinese fir cell wall. HIMW treatment can produce different characteristics of wood cracks. The size and number of cracks were significantly increased with the increase in MWED, and more cracks were found in low MC. Microcracks caused by HIMW treatment tended to initiate at the ray parenchyma, resulting in the stripping of ray cells along its radial direction. Meanwhile, the cracking of adjacent cell junctions, the rupturing of the pit margo and pit torus, and cell wall parts tearing along the direction of microfibrils occurred as a result of the HIMW treatment. The most severe damage to the cell walls occurred at the interface of S1/S2, S1, and ML layers, and the cell walls were torn in the S2 layer. There were no significant changes in the FTIR spectra of the HIMW treatment samples. Hemicellulose degradation occurred first, which increased with the increase in MWED. The recrystallization of cellulose and the lignin content increased because of the change in the aromatic C=O groups. As MWED increased, both the crystallinity index (CI) and cellulose crystal width (D_{200}) of the samples that underwent HIMW treatment increased accordingly, and the number of low-MC samples was greater than that of the high-MC samples. The findings contribute to understanding the crack characteristics and damage mechanism induced by HIMW treatment on wood. This study provides valuable insights into regulating the effects of HIMW treatment and expanding its application in wood processing, such as wood drying and functionalized impregnation, according to the specific end-use requirements.



Citation: Liao, X.; Fang, X.; Gao, X.; Yi, S.; Zhou, Y. Effect of High-Intensity Microwave Treatment on Structural and Chemical Characteristics of Chinese Fir. *Forests* **2024**, *15*, 516. <https://doi.org/10.3390/f15030516>

Academic Editor: Chunping Dai

Received: 2 February 2024

Revised: 1 March 2024

Accepted: 5 March 2024

Published: 11 March 2024



Copyright: © 2024 by the authors. Licensee MDPI, Basel, Switzerland. This article is an open access article distributed under the terms and conditions of the Creative Commons Attribution (CC BY) license (<https://creativecommons.org/licenses/by/4.0/>).

Keywords: microwave; Chinese fir; wood structure; cell wall

1. Introduction

Chinese fir [*Cunninghamia lanceolata* (Lamb.) Hook] is a widely cultivated and fast-growing wood species in China. However, it has inherent drawbacks, such as low density, weak strength and stiffness, susceptibility to biological decay, poor dimensional stability, poor permeability in heartwood, and a tendency to crack during drying [1]. These

limitations make it unsuitable for direct use in furniture, flooring, wooden structures, and construction [2]. Consequently, there is a need to enhance the quality of Chinese fir wood for its broader application across the wood industry [3]. One common approach is to improve its permeability, especially in the heartwood, to facilitate drying and impregnation.

Fluid flow within softwood occurs through three primary pathways. Longitudinally, fluid flow moves through the lumina of the tracheid, the apertures of pits, and the micropore of bordered pit membranes [4,5]. In the tangential direction, fluid flow primarily occurs through tracheids, bordered pits, and ray cells serving as the main radial pathways [6,7]. Additionally, a microcapillary system within tracheid cell walls allows fluid penetration in longitudinal, tangential, and radial directions [8]. Enhancing wood permeability involves opening up these primary fluid pathways.

Microwave treatment is an effective and environmentally friendly method for wood drying and pretreatment before modification, with successful industrial applications [9,10]. HIMW treatment, in particular, provides a greater amount of energy, resulting in higher temperature and steam pressure within the wood in a shorter period of time [9]. The use of continuous feeding devices in HIMW treatment increases efficiency and overcomes the limitations of conventional methods, which struggle to achieve desired treatment effects on large specimens [9–11]. The effectiveness of microwave treatment depends not only on specific parameters such as power, energy application mode, pulse or continuous treatment, exposure time, and speed of timber movement but also on factors like wood species, initial MC, and sample dimensions [9–13].

Under high-intensity irradiation, the water present in wet wood absorbs electromagnetic energy and rapidly evaporates, generating high internal vapor pressure within the wood cells. This pressure leads to the formation of cracks and micro-cracks in the thin-walled cells, creating new pathways for fluid flow and increasing the permeability of the wood [9,12,14–16]. Torgovnikov and Vinden [9] categorized the modification of softwood into three degrees based on the extent of cell damage. A low degree of modification included the rupturing of pit membranes of wood cells and the melting and replacement of resin in channels. At a moderate degree, the pit membranes and ray parenchyma cells underwent further rupturing, and resin underwent boiling and replacement. At a high degree, the primary cell wall of the wood ruptured, including the ray parenchyma cells and tracheids, and cavities formed in the wood. The level of damage varied depending on the processing parameters and wood sample condition.

Low-intensity microwave treatment can cause the middle lamellar between ray parenchyma cells and longitudinal tracheids to crack, bordered pit membranes in the tracheids cell wall to become damaged, and micro-fibrils on the pit margo to rupture. Furthermore, micro-cracks were discovered in cross-field pit apertures, and the aspirated pit was slightly opened [14,16,17]. When the microwave intensity or processing time increased, the pit border separated from the tracheid cell wall, both the pit margo and the pit torus were broken thoroughly, and cracks appeared in the tracheid cell wall along the direction of microfibrils. Meanwhile, the cross-field pit membranes disappeared, the ray parenchyma cells were seriously damaged, the tracheid walls were fractured, and macro-cracks were generated [14–16]. HIMW treatment can cause changes in the chemical composition of wood, including hemicellulose, lignin, and cellulose. The crystallinity and cellulose crystal width of the wood cell wall fluctuated with microwave treatment [18]. While some studies have investigated the structural damage of wood during microwave treatment, there is limited research on the changes in the cell wall. The cell wall, which serves as the fundamental component and primary structure of wood, is a thin layer formed through the deposition of cellulose, hemicellulose, and lignin according to specific biological mechanisms. It consists of multiple layers, including the primary wall (P) and secondary wall (S1, S2, and S3 layers), with adjacent cell walls connected by a middle lamella (ML) [19,20].

Despite the known potential for microwave treatment to cause damage to the macro- and microstructure of wood, most studies have focused on the damage to intercellular and tissue cell types. Limited research has been conducted on cell wall damage location

and the chemical structure following microwave treatment. However, it is important to understand that the macroscopic properties of wood are largely influenced by the cell wall structure and properties at the microscopic level. The macroscopic destruction observed in wood results from the cumulative damage to the cell wall. Therefore, investigating the destruction of the cell wall plays a crucial role in understanding the macroscopic damage of wood. It is crucial to study and elucidate the structural damage and property changes that occur in the wood cell wall during HIMW treatment. Therefore, the objectives of this research were to examine the morphology and size of macroscopic cracks in Chinese fir wood treated with HIMW and analyze the changes in crack morphology and chemical structure at the cell wall level.

2. Materials and Methods

2.1. Materials

The wood used in this study was obtained from fast-growing Chinese Fir. These logs were sourced from a forest farm in Congjiang County, Guizhou Province, China. The diameter of the trunk at breast height was over 40 cm, and the rotation of the trees was about 30 years. The logs were sawn into wood planks with dimensions of $2200 \times 120 \times 50 \text{ mm}^3$ (longitudinal \times tangential \times radial, $L \times T \times R$). The treated samples with dimensions of $1200 \times 120 \times 50 \text{ mm}^3$ were obtained from these planks, while the remaining planks were used as control samples. To ensure uniformity, the initial MC of the samples was adjusted to two groups: low MC (L) ranging from 30% to 60%, and high MC (H) ranging from 60% to 90%. The average oven-dry density of the wood was measured as 0.35 g/cm^3 .

2.2. High-Intensity Microwave (HIMW) Treatment

The microwave treatment was conducted using continuous feeding high-intensity microwave equipment (WXD 200 L; Sanle, Nanjing, China). This equipment operates at a frequency of 915 MHz and offers adjustable power ranging from 1 kW to 200 kW. The feeding speed can be step-less adjusted between 0.6 m/min and 6 m/min. The resonant cavity of the equipment has dimensions of $550 \times 340 \times 280 \text{ mm}^3$ (length \times width \times height), and the microwave energy is emitted from four feed ports of the resonant cavity, with a maximum power of 25 kW at the upper and lower feed port and 75 kW at the left and right feed port (Figure 1b).

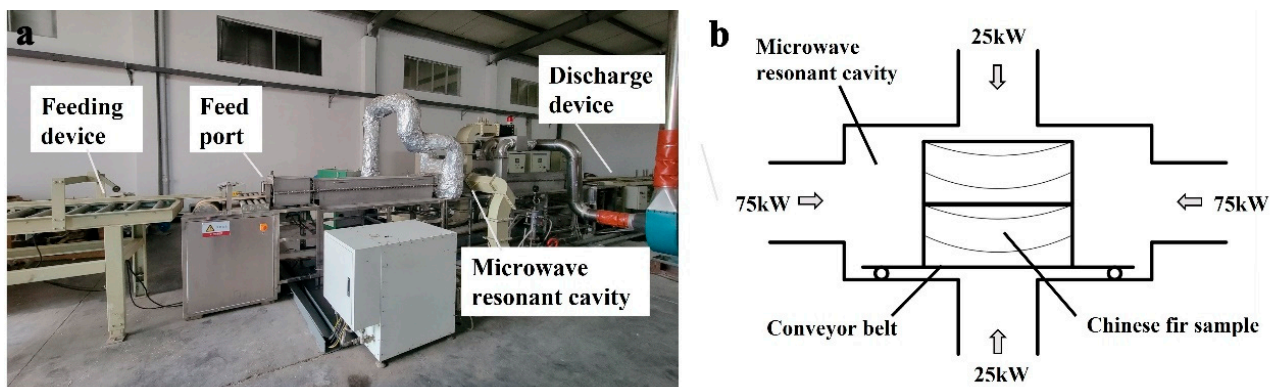


Figure 1. WXD200L microwave equipment. (a) Photograph of microwave equipment. (b) Four feed port of microwave resonant cavity.

Microwave energy density (MWED) was utilized to quantify the energy absorbed by the samples. MWED represents the energy absorbed per unit volume of the wood sample, and it is influenced by the sample's volume within the microwave radiation, the microwave power, and the duration of exposure. The MWED can be calculated using Equation (1):

$$M = \frac{E}{V} = P \cdot \frac{t}{V} = P \cdot \frac{(l/v)}{V} \quad (1)$$

where M is the microwave energy density in microwave processing (kWh/m^3); E is the microwave energy absorbed by wood (kWh); V is the volume of wood irradiated by microwaves (m^3); P is the microwave power absorbed by wood (kW); t is the processing time in microwave resonance cavity (h); l is the length of the microwave resonant cavity (m); and v is the wood-feeding speed (m/h).

In this study, a microwave input power of 60 kW, 80 kW, and 100 kW, a feeding rate of 1.0 m/min, and a processing duration of 33 s were employed. During microwave processing, it is noted that not all input MWED was absorbed; a portion was reflected back and absorbed by the water load-bearing MW source. To avoid serious cracks caused by HIMW, two planks were stacked feeding during treatment (Figure 1b). The effective energy density acting on the sample was determined by measuring the power absorbed and the reflected power (Table 1).

Table 1. The energy density of Chinese fir during HIMW treatment.

Input Power (kW)	Reflected Power (kW)	Absorbed Power (kW)	Effective MW Energy Density (kWh/m^3)
60	17.9	42.1	58
80	22.28	57.72	80
100	27.81	72.19	100

2.3. Macroscopic Observation

To evaluate the surface checks of Chinese fir samples subjected to HIMW treatment, photographs were captured employing a GR3 camera (Ricoh, Tokyo, Japan). Subsequent analysis and quantification of the surface checks were performed utilizing using ImageJ 1.54d software.

2.4. Optical Microscope Observation

Samples with a dimension of $5 \times 2 \times 2 \text{ mm}^3$ ($L \times T \times R$) were prepared from the HIMW treatment samples and the control samples. These samples underwent dehydration using a graded series of acetone and were subsequently embedded in Spurr's low-viscosity resin. Transverse semi-thin sections, approximately $1 \mu\text{m}$ thickness, were obtained from the embedded samples by a glass cutter and mounted on glass slides. These sections were stained with a 1% w/v solution of toluidine blue in 0.1% boric acid on a hot plate at approximately $60 \text{ }^\circ\text{C}$. The stained sections were then observed under an optical microscope (Axio scopeA1; Zeiss, Oberkochen, Germany) to capture the images for analysis.

2.5. Scanning Electron Microscope (SEM) Observation

Samples measuring $5 \times 5 \times 5 \text{ mm}^3$ ($L \times T \times R$), extracted from the center position of both the HIMW-treated specimens and the control, were prepared for observation under SEM. Transverse sections (TS), radial longitudinal sections (RLS), and tangential longitudinal sections (TLS) of the samples were prepared by trimming with a microtome (M205C; Leica, Frankfurt, Germany). The trimmed sections were subsequently subjected to adjustment under constant temperature and humidity conditions. Subsequently, they were dried in an oven at $60 \text{ }^\circ\text{C}$ until a constant weight was achieved. To enhance the conductivity, the sections were coated with gold (Au) using a coating device (Quorum SC7620; East Sussex, UK). The coated sections were then observed using an SEM (ZEISS Gemini 300; Zeiss, Oberkochen, Germany).

2.6. Transmission Electron Microscope (TEM) Observation

The samples used for TEM observation were identical to those for optical microscopy. Transverse ultrathin sections, approximately 70 nm thickness, were obtained from the embedded samples using an Ultramicrotome (EM UC7; Leica, Frankfurt, Germany) with histology diamond knives. Following the sectioning process, the ultrathin sections were transformed into copper mesh grids. These grids were then stained with lead citrate and

a 50% ethanol-saturated uranyl acetate solution for 5–10 min each. Finally, the stained sections were observed using TEM equipment (Hitachi7650, Ltd., Tokyo, Japan), which ran at an acceleration voltage of 80 kV.

2.7. Fourier-Transform Infrared Spectroscopy (FTIR) Analyzing

The samples were first ground into a powder using a grinder. The resulting material was then screened through a 200 mesh sieve and dried at 60 °C until a constant weight for analysis. Dried powder samples were analyzed using an FTIR spectrometer (Nicolet 6700; Nikola, Boston, MA, USA) in transmission mode to obtain the FTIR spectra. The spectra were collected in the wave number range of 4000–400 cm^{-1} , with 32 scans performed at a resolution of 4 cm^{-1} . To ensure accurate analysis, the FTIR spectra were baseline-corrected using software at specific wave numbers 1800 cm^{-1} , 1548 cm^{-1} , and 840 cm^{-1} .

2.8. X-ray Diffraction (XRD)

The relative crystallinities of the dried powder samples, which were 100–200 mesh size, were determined using an X-ray powder diffractometer (D8 Advance; Bruker, Ettlingen, Germany). $\text{CuK}\alpha$ radiation ($\lambda = 1.541 \text{ \AA}$) was employed at 40 kV and 40 mA. To conduct the test, the powder samples were placed in a sample box, flattened, and positioned horizontally within the instrument. Intensity measurements were taken in the range of $5^\circ < 2\theta < 40^\circ$, with a scan step size of 0.05° and a scanning speed of $0.1^\circ/\text{s}$. The crystallinity index (CI) was calculated using Equation (2) [21]:

$$CI = \frac{I_{002} - I_{\text{am}}}{I_{002}} \times 100\% \quad (2)$$

where CI expresses the relative degree of crystallinity; I_{002} is the intensity of the crystalline peak at $2\theta = 22.2^\circ$; and I_{am} is the height of the minimum between the 200 and 101 peaks at $2\theta = 18.6^\circ$. Three measurements were performed for each sample group.

The width of the crystallite was determined using the Scherrer equation, which relies on the measurement of the diffraction fringe width of the X-ray reflection in the crystal region. Specifically, the crystalline size D_{200} was calculated based on the diffraction pattern obtained from the 200 lattice planes of cellulose, using Equation (3):

$$D_{200} = \frac{K\lambda}{\beta \cos \theta} \quad (3)$$

where D_{200} is the average size of the crystallites; K is the Scherrer constant ($K = 0.9$); λ is the X-ray wavelength ($\lambda = 0.1541 \text{ nm}$); β is the peak width of the (200) profile at half maximum (FWHM) in radians; and θ is the half of the (200) Bragg diffraction peak position in radian [22].

3. Results and Discussion

3.1. Macroscopic Surface Cracks Analysis

The wood samples subjected to HIMW treatment exhibit surface cracks, the number and size of which vary depending on different process parameters. To analyze these surface cracks, photographs were captured using a camera, and the original images were subsequently converted into grayscale and processed for edge detection using ImageJ software (refer to Figure 2). The edges of the cracks were identified and quantitatively measured to determine their length and width.

The number of surface cracks and the corresponding length and width of each crack after HIMW treatment are shown in Figure 3. The number of surface checks increases with higher MWED values. When the MWED was 80 kWh/m^3 , the number of cracks increased sharply, and the crack size of the high MC group was larger than that of the low MC group. While the MWED was increased to 100 kWh/m^3 , samples with lower MC exhibited more surface cracks than those with higher MC. As presented in Table 2, when the MWED ranges

from 58 kWh/m³ to 100 kWh/m³, and the MC of the sample is lower, the average length of cracks increases from 28.69 mm to 49.27 mm, a rise of 71.7%. Similarly, the mean width of the widest crack nearly doubles from 0.123 mm to 0.240 mm. Conversely, when the MC of the sample is higher, the average length of cracks increases from 20.28 mm to 44.30 mm, representing a substantial increase of 118.4%. Additionally, the average width grows from 0.15 mm to 0.199 mm, a rise of 32.7%.

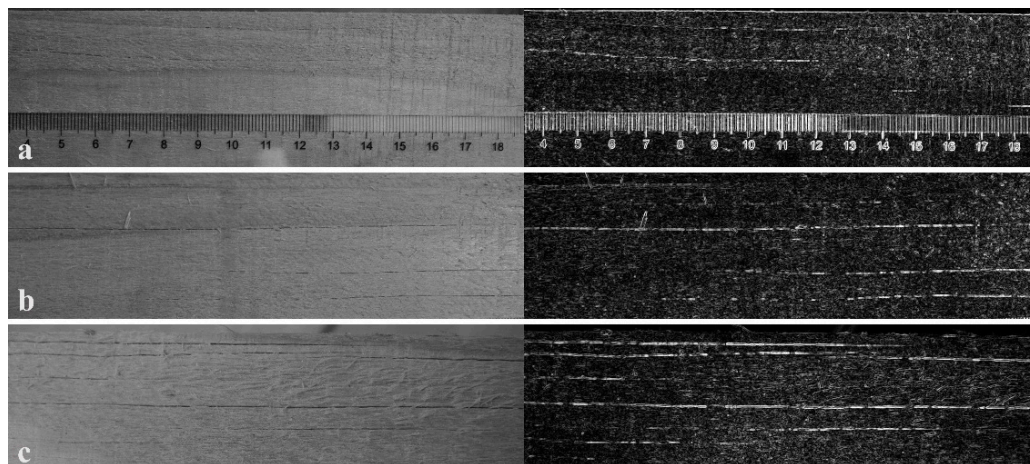


Figure 2. Surface cracks caused by HIMW treatment. (a) MWED is 58 kWh/m³, and the initial MC is 53% (58 L). (b) MWED is 80 kWh/m³, and the initial MC is 48% (80 L). (c) MWED is 100 kWh/m³, and the initial MC is 47% (100 L).

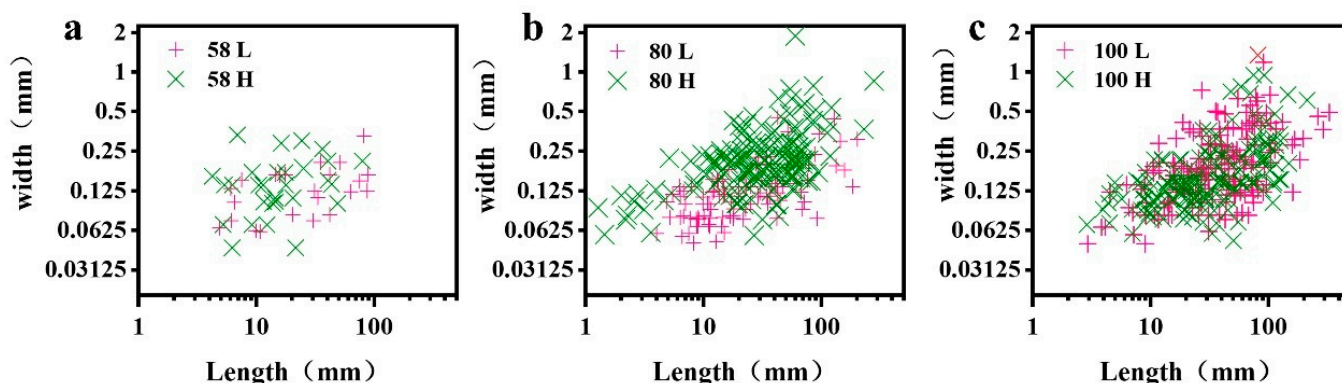


Figure 3. Characteristic of surface cracks caused by HIMW treatment. (a) The MWED is 58 kWh/m³. (b) The MWED is 80 kWh/m³. (c) The MWED is 100 kWh/m³.

Table 2. Surface cracks characteristic of HIMW treatment.

Samples	Width/mm	Length/mm	Length Proportion of Totality/%				Width Proportion of Totality/%			
			Below 10 mm	10–40 mm	40–80 mm	Above 80 mm	Below 0.1 mm	0.1–0.2 mm	0.2–0.4 mm	Above 0.4 mm
58 L	0.123 ± 0.056	28.69 ± 23.09	28.9	44.4	20.0	6.7	42.2	55.6	2.2	0
58 H	0.150 ± 0.073	20.28 ± 16.84	27.6	57.2	17.2	0	17.2	62.1	20.7	0
80 L	0.130 ± 0.067	31.82 ± 34.43	24.7	49.5	17.9	7.9	34.7	52.6	11.6	1.1
80 H	0.245 ± 0.191	40.55 ± 35.85	11.5	46.5	45.8	7.7	7.7	36.8	44.5	11
100 L	0.240 ± 0.194	49.27 ± 46.37	9.3	43.5	32.3	14.9	15.5	38.8	32	13.7
100 H	0.199 ± 0.171	44.30 ± 37.18	12.8	47.7	25.6	13.9	15.1	52.9	24.4	7.6

The length and width of the cracks observed were categorized into four grades, and the proportion of each grade to the total number of cracks was determined. The length of cracks

was categorized into below 10 mm, 10–40 mm, 40–80 mm, and above 80 mm, and the width was categorized into below 0.1 mm, 0.1–0.2 mm, 0.2–0.4 mm, and above 0.4 mm (Table 2). The number of cracks in each grade was counted as a percentage of the total number of cracks. In the case of MWED ranging from 58 kWh/m³ to 100 kWh/m³, particularly evident in the 80 H (MWED is 80 kWh/m³ and high MC) group, there was a significant decrease in the proportion of cracks with lengths below 10 mm. Conversely, the proportion of cracks with lengths above 40 mm was substantially increased. The proportion of the grades in 10–40 mm was not significant. Furthermore, significant differences were observed in the proportion of cracks with a width below 0.2 mm, especially widths below 0.1 mm, in the 58 L (MWED is 58 kWh/m³ and low MC) group and 80 L group compared to other groups. With an increase in MWED, the proportion of cracks with widths above 0.2 mm substantially increased, indicating an increase in the number of larger cracks in the groups above 80 H group.

The occurrence of wood cracks is affected by the initial MC of the sample, where samples with a lower MC demonstrate an increased likelihood of crack formation. This phenomenon can be attributed to the rapid heating rate within the wood, which accelerates the evaporation process, resulting in a significant pressure differential between the internal and external environments of the wood. Such a differential facilitates the easy formation of cracks within the wood structure. In contrast, the heating rate of wood with a higher MC was slow because the microwave energy is absorbed by the excess water; meanwhile, it exhibits a more uniform internal heating temperature [14,23]. When comparing samples with the same MC, increased energy absorption correlates with a reduced duration required for water evaporation, resulting in higher steam pressure and a greater destructive power force upon the wood's structure. Consequently, internal structural damage extends to the surface, giving rise to cracks [9].

3.2. Damage in Cell Wall Analysis

3.2.1. Optical Microscope Analysis

To analyze the damage patterns characterized by cell wall cracking, samples treated with HIMW were subjected to detailed observation through optical microscopy and TEM techniques. These observations were conducted on semi-thin and ultra-thin sections to facilitate a comprehensive analysis of the cell wall structural alterations induced by the treatment. As shown in Figure 4, it can be observed that when Chinese fir is treated with HIMW, the initial damage location often occurs near the wood ray. Cracks form along the radial wood rays, and there appears to be separation and peeling between the ray cells and tracheids (Figure 4a). When the MWED reaches 80 kWh/m³, the cracks in the radial wood rays widen further, and the tracheids near the ray cells separate and extend along the tangential direction (Figure 4b). This is mainly due to the fact that the ray cells are parenchyma cells, which absorb microwave energy and rapidly heat up, generating vapor pressure that impacts and destroys the intercellular layer of the ray cells with lower intensity [9,14]. With an increase in MWED to 100 kWh/m³, the separation between tracheids is further expanded, and cracks typically start at one wood ray and end at another ray (Figure 4c). This is primarily caused by initial fracture cracks occurring in the tracheid of the cross-field region, resulting in transverse wall breakage. The cross-field region is prone to rupture because the microfibril of wood rays and tracheids cell walls are arranged in different directions [16].

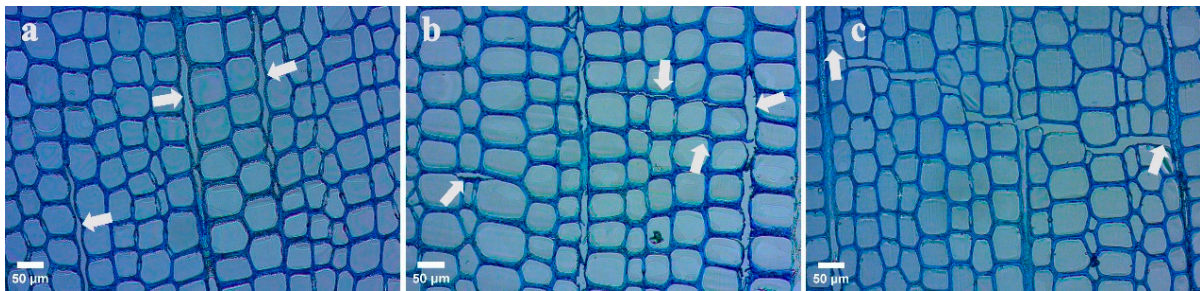


Figure 4. Semi-thin section images of HIMW-treated specimen. (a) TS plane of HIMW (60 L) specimen. (b) TS plane of HIMW (80 L) specimen. (c) TS plane of HIMW (100 L) specimen. The arrows in the figures indicate the location of the damage.

3.2.2. SEM Analysis

Figure 5 presents SEM observations of the sections (TS, RLS, TLS) of the control and HIMW treatment specimens. In the TS plane of the control specimens (Figure 5a), the integrity between the tracheids and wood rays is clearly observed. However, distortion is evident in the HIMW treatment specimens (Figure 5b), and there is a gap of approximately 30 μm in the wood ray position. Notably, the cell wall separation between the tracheids often occurs near the wood rays (Figure 5c). The ray parenchyma cells, being structurally weaker, are initially damaged during the HIMW treatment process [18].

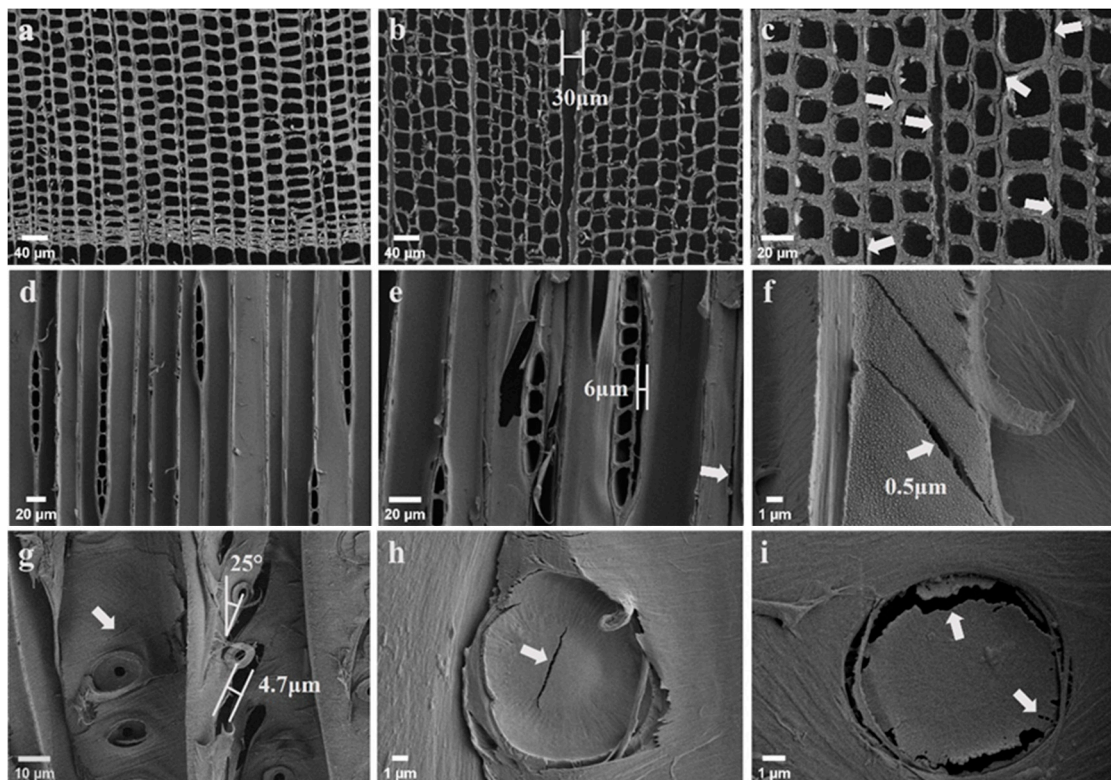


Figure 5. SEM images of control and HIMW-treated specimen. (a) TS of control specimen. (b) TS of HIMW (80 L) specimen. (c) TS of HIMW (80 L) specimen. (d) TLS of control specimen. (e) TLS of HIMW (80 L) specimen. (f–i) RLS of HIMW (100 L) specimen. The arrows in the figures indicate the location of the damage.

These observations were also noted in the TLS plane, where the MWED was 80 kWh/m^3 . It was observed that the intermediate lamellae between the ray parenchyma cells and the longitudinal tracheids were cracked (Figure 5e); meanwhile, in the control specimens, integrity was maintained (Figure 5d). Furthermore, the compound middle lamella (CML)

between the tracheids exhibited tears and micro-cracks (Figure 5e). These phenomena can be attributed to the vapor pressure generated by the rapid evaporation of water inside the wood [17,24]. Upon further increasing the MWED to 100 kWh/m³, a portion of the weakened tracheid walls were torn, and the cracks propagated along the direction of microfibrils, which are parallel to the microfibril angle of the S2 layer of the wood cell wall. The crack tilt is approximately 25° (the microfibril angle of the S2 layer of Chinese fir is typically 25–30° away from the fiber axis [25]) (Figure 5f). These cracks also occurred in the bordered pit (Figure 5g), leading to a rupture of the bordered pit into a 4.7 µm width crack along the microfibrils of the S2. This finding may be attributed to the physical and chemical properties of the S2 layer, which are believed to dominate the cell wall [14,24]. In wood fiber materials, compared to those in the parallel direction, the strength and stiffness values perpendicular to the wood fiber direction are lower [26]. Consequently, it is more likely to experience vertical breakage under steam pressure. The adjacent microfibrils separate, resulting in the formation of cracks that propagate along the orientation direction of the microfibrils.

In the heartwood of Chinese fir, the bordered pit membranes are typically covered with amorphous materials, resulting in the pit membrane being completely encrusted and blocking the micropores on the pit margo. This significantly hinders permeability [27]. Additionally, the pit torus (Figure 5h) and pit margo (Figure 5i) were also ruptured and cracked due to the HIMW treatment. The HIMW treatment can also dissolve the amorphous materials on the pit margo, expose the numerous interwoven microfibrils, and increase the number and diameter of the pores. The high-pressure vapor formed within the lumen of the tracheid cell had difficulty escaping through the closed migration paths (pit aspiration). Consequently, the vapor pressure may lead to cracks in the weak region formed by closely aligned bordered pits [14,17].

3.2.3. TEM Analysis

To further examine the damage to the cell wall layer, TEM was utilized to observe the cell wall damage (Figure 6). The TEM image reveals detailed cracks on the cross-section of the fractured tracheid. Comparing it with the control specimen (Figure 6a), it is evident that the interface debonding occurs at the S1/S2 interface, splitting at the S1 layer and CML (Figure 6b). This may be attributed to the microfibril angles being completely different in the S1 layer and S2 layer and the irregular arrangement angle of the microfibrils in the S1 layer. Additionally, cracks in the S2 layer of the cell wall are roughly torn (Figure 6c). This indicates that the cracks observed under SEM are mainly due to the tearing of the S2 layer in the tracheid cell wall (refer to Figure 5f,g). It is speculated that the fracture process of the tracheid wall initiates from the fracture of the S1/S2 interface and S1, and then the crack extends to the S2 layer (Figure 6c).

The bordered pit of Chinese fir has aspirated pits (Figure 6d), and the impermeable pit torus blocks the path between tracheid cells, significantly affecting breathability. The pit margo, a reticular structure composed of numerous interwoven microfibrils, facilitates fluid flow between adjacent tracheids through its micropore pore structure [28]. The vapor pressure generated by HIMW causes the pit margo to break and dissolve, leading to some pit torus resilience. Additionally, HIMW treatment can result in the tearing of the pit border (Figure 6e). The direction of the arrangement of the microfibrils near the bordered pit was different. The microfibrils are arranged to detour the pit aperture, and the cracks extend along the edge of the pit aperture.

HIMW treatment of wood aims to enhance permeability, which can be effectively achieved by introducing appropriate cracks. Analyzing and measuring the morphology of these cracks can serve as an evaluation criterion for assessing the effectiveness of microwave treatment. By carefully examining the cracks, the appropriate energy density can be chosen for processing based on the intended use of the wood.

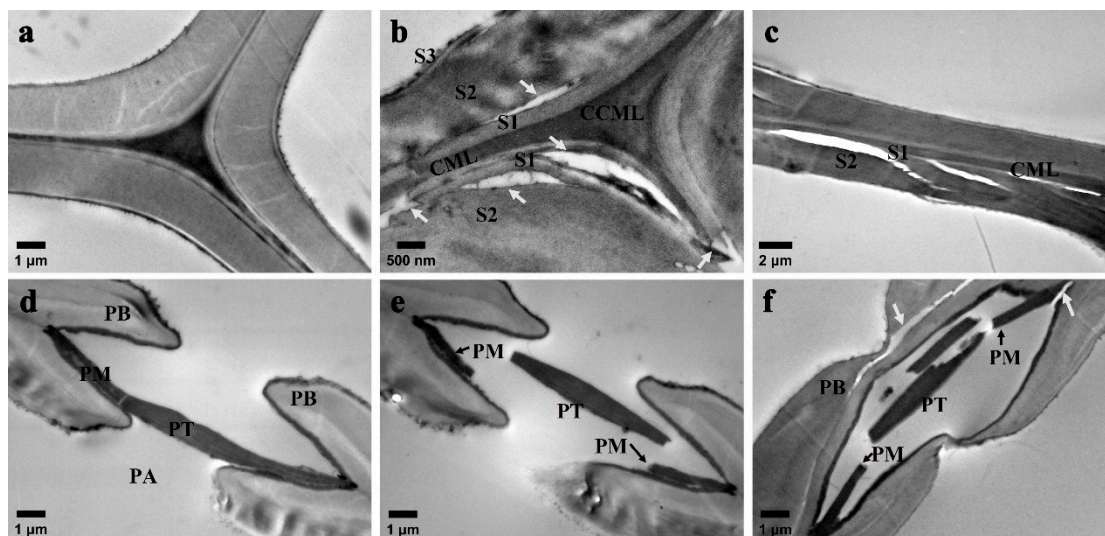


Figure 6. TEM images of cross-sections of control and HIMW treatment specimens, taken at 80 kV. (a) Cell wall of control. (b,c) Cell wall of HIMW treatment (100 L). (d) Bordered pit (aspirated pit) of control. (e,f) Bordered pit of HIMW treatment (100 L). CCML: cell corner middle lamella between adjoining tracheids; CML: compound middle lamella (P and ML); S1: outer secondary wall; S2: middle secondary wall; S3: inner secondary wall; PT: pit torus; PM: pit margo; PB: pit border; PA: pit aperture. The arrows in the figures indicate the location of the damage.

3.3. FTIR Spectroscopy Analysis

Wood cell walls are primarily composed of cellulose, hemicellulose, and lignin, with the chemical component significantly influencing the properties of wood [29]. Degradation of wood material commences when its temperature exceeds 100 °C, a process that significantly affects the primary chemical composition of the cell wall [23]. HIMW treatment employs high-temperature steam heating of the wood, which can induce alterations in the chemical structure of the cell wall. Furthermore, the non-thermal effects of microwaves also affect the structure of the treated sample [30,31].

The chemical functional groups of wood and their corresponding FTIR peaks are listed in Table 3. The absorption peaks at 1605 cm^{-1} , 1510 cm^{-1} , and 1268 cm^{-1} are associated with characteristic stretching or bending vibrations in different lignin groups, and the absorption peaks at 1425 cm^{-1} , 1371 cm^{-1} , 1317 cm^{-1} , and 896 cm^{-1} correspond to cellulose groups. Additionally, the absorption peaks at 1736 cm^{-1} and 810 cm^{-1} are assigned to hemicellulose groups [32–34].

Table 3. Chemical functional group and corresponding FTIR peaks.

Assignment	FTIR Peak (cm^{-1})	Functional Group
Hemicellulose	810	Glucomannan in softwood
Cellulose	896	C–H bending and asymmetric out-of-plane ring stretching
Lignin	1268	C–O stretching vibrations of the methyl and phenyl propane units
Cellulose	1317	CH ₂ wagging
Cellulose	1371	C–H bending vibrations in polysaccharides
Cellulose	1425	C=C aromatic skeleton vibration and CH ₂ bending vibration
Lignin	1510	C=C stretching of the aromatic ring
Lignin	1605	C=O stretching vibration and C=C aromatic ring vibration
Hemicellulose and xylan	1736	C=O stretching of acetyl or carboxylic acid

Figure 7 displays the average FTIR absorbance spectra of HIMW treatment and control samples in the 1800–800 cm^{-1} fingerprint region. All spectra were normalized at 1025 cm^{-1} . Compared to the control samples, the chemical structure of the HIMW treatment samples exhibited slight changes in the wood cell wall. By analyzing the trends of characteristic peaks of cellulose, hemicellulose, and lignin, it was observed that different chemical components displayed different responses to HIMW treatment.

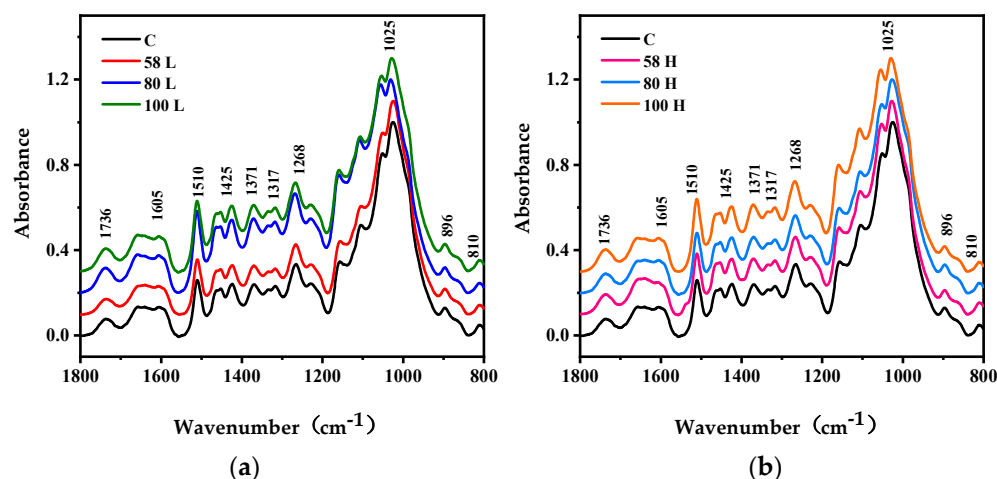


Figure 7. FTIR spectra of the wood cell wall of control and HIMW treatment specimens. (a) FTIR spectra of low MC and control specimens. (b) FTIR spectra of high MC and control specimens.

At 1736 cm^{-1} and 810 cm^{-1} , the absorbance intensity of the HIMW treatment samples was higher than that of the control samples, indicating the destruction of carbonyl and acetyl groups in xylan and glucomannan. These absorption peaks correspond to the stretching vibrations of the carbonyl group (C=O) in the xylan branch chain and glucomannan in softwood [30] (Table 3). When the MWED was 60 kWh/m^3 for both low and high MC samples, no notable changes in absorbance intensity were observed between the HIMW treatment and control samples. However, at MWEDs of 80 kWh/m^3 and 100 kWh/m^3 , the absorbance intensity of the low MC hemicellulose peak showed an overall increase (Figure 7a), while the changing trend in the high MC sample was not evident (Figure 7b). This could be attributed to the negative impact of a large amount of free water on temperature rise.

Regarding cellulose, the absorbance peaks at 1317 cm^{-1} , 1371 cm^{-1} , 1425 cm^{-1} , and 896 cm^{-1} are associated with oscillating vibrations of CH_2 in crystalline cellulose, bending vibrations of C–H in polysaccharides, and plane bending vibrations of O–H in amorphous cellulose, respectively. These peaks are used to evaluate the structural changes in cellulose [35,36]. Due to its high thermal stability and relatively compact structure, cellulose experienced minimal damage, increasing cellulose adsorption slightly at 1317 cm^{-1} and 1425 cm^{-1} . However, with the increase in MWED, especially at 80 kWh/m^3 and 100 kWh/m^3 , cellulose underwent a change under high-temperature conditions. This may be caused by the non-thermal effects of microwaves [30].

The absorbance peaks at 1268 cm^{-1} , 1605 cm^{-1} , and 1510 cm^{-1} in lignin exhibit elevated levels across most spectra. These changes in peak intensity are attributed to alterations in the relative content of lignin. The absorption peak at 1510 cm^{-1} shows a significant increase in HIMW treatment wood samples compared to the control, particularly at low MC, MWED is 80 kWh/m^3 and 100 kWh/m^3 . This increase is due to the degradation of other components and the rise in the relative content of the aromatic skeleton, which is caused by a complex combination of microwave and hygrothermal effects [37]. On the other hand, the characteristic absorption peaks at 1268 cm^{-1} and 1605 cm^{-1} only show slight increases after HIMW treatment, indicating complex structural changes within guaiacyl lignin and side chains [38]. The change in the chemical composition of cellulose, hemicel-

lulose, and lignin are caused by the HIMW treatment. These may affect the physical and mechanical properties of wood and the crosslinking of impregnation modifier. However, further research is needed to understand the specific structural components of cell wall chemistry affected by HIMW treatment.

3.4. Cellulose Crystalline Structure Analysis

The hemicellulose and lignin present in wood are characterized by their amorphous nature, whereas cellulose consists of both amorphous and crystalline regions. The crystalline structures of cellulose are relatively small in size. The thermal stability, mechanical strength, hardness, density, and hygroscopicity of wood are significantly impacted by the structure of crystalline and the amorphous regions within cellulose [39].

Crystallinity is a crucial parameter that measures the proportion of crystalline regions compared to amorphous content in a material [40]. In this study, XRD was employed to investigate changes in the crystallinity of wood, as well as the crystal width of cellulose crystallites [41]. Variations in the intensity of the diffraction bands indicated alterations relative to crystallinity. The peak near $2\theta = 22^\circ$, corresponding to the crystallographic plane with a Miller index of (200), was commonly used to assess the crystallinity of the samples [35,42]. A moderate peak was observed at around 34.5° , which belonged to the (040) crystallographic plane, which was not the dominant contributor [43].

The HIMW treatment did not induce any changes in the crystal structure of Chinese fir cellulose, as evidenced by similar XRD patterns observed in both treated and control samples (Figure 8a). The HIMW treatment samples did not exhibit noticeable alterations in the number or position of reflection peaks compared to the control sample, indicating the absence of crystal-type transformations during the HIMW treatment. However, under different conditions, the intensity and width of the (200) reflection peaks in the treated samples changed, indicating some crystallinity modifications. Furthermore, a decrease in the diffraction intensity of amorphous regions near 2θ of 18.6° was observed in the samples after HIMW treatment, which is attributed to amorphous scattering in cell walls. Interestingly, the HIMW treatment significantly enhanced the diffraction of the amorphous regions of cellulose, resulting in a higher degree of crystallinity in the treated samples.

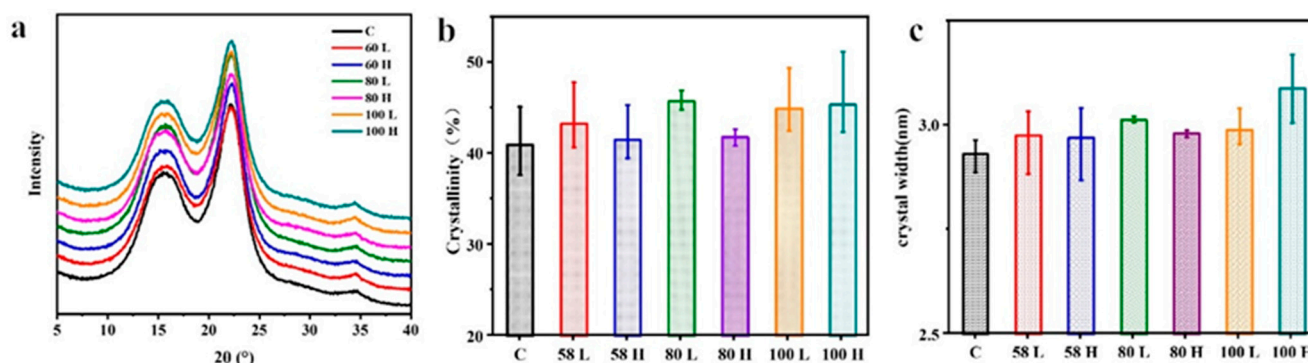


Figure 8. The cellulose crystalline structures of the control and HIMW treatment specimens. (a) X-ray diffractograms. (b) The relative crystallinities. (c) Crystal width.

Figure 8b illustrates that the control sample has a crystallinity index (CI) value of 41.03%. As the MWED increased, the CI value of the treated samples increased compared to the control samples. When the MWED is increased from 58 kWh/m³ to 100 kWh/m³, the mean CI of the low MC sample and that of the sample with the high MC sample exhibit an increase of 3.83% and 9.29%, respectively. The reduction in the amorphous cellulose region was the main reason for the increase in CI of HIMW treatment samples. At the same MWED, except for the group of 100 kWh/m³, the crystallinity of the low MC sample is higher than that of the high MC sample because the sample with low MC obtains a higher temperature in a short time during HIMW treatment. This is a contribution to the thermal

effect of microwaves. This increase in crystallinity can be attributed to the decomposition of amorphous regions in cellulose and hemicellulose, as well as the crystallization of amorphous cellulose resulting from thermal degradation [44,45]. Additionally, the non-thermal effect of dielectric relaxation induced by microwaves leads to a change in the initial distance between hydroxyl groups due to variations in hydrogen bonding degrees of freedom. This, in turn, promotes the recrystallization of cellulose to some extent [46].

Figure 8c depicts the changes in the crystal width of cellulose in the HIMW treatment and control samples. The average D_{200} value of the control sample is 2.93 nm and is lower than that of the HIMW treatment samples. When the MWED is 100 kWh/m³, the average D_{200} values of the low and high MC samples increased to 2.99 nm and 3.09 nm, resulting in a 2.05% and 5.46% increase, respectively. This phenomenon can be attributed to hydrothermal processes that rapidly weaken the cellulose molecular chains and improve mobility [46]. The exposure of cellulose to HIMW facilitates the reorganization and recrystallization processes, enhancing the volume and degree of microfibril aggregation, ultimately increasing cellulose's crystallinity and crystal width [47,48].

4. Conclusions

This study focused on the crack morphology, damage position, and chemical composition changes in the cell wall of Chinese fir via HIMW treatment. The results showed the MC of the wood and the MWED played significant roles in influencing the crack morphology. When the MWED is 58 kWh/m³ with low MC and high MC and 80 kWh/m³ with low MC, the proportion of cracks with a length below 40 mm and width below 0.2 mm is more than 70% and 80%, respectively. Morphological observations revealed that as the MWED increased, so did the maximum crack's width and length. Additionally, the low MC in the wood caused more cracks, and the higher MC in the wood resulted in more uniform cracks. HIMW treatment induced various types of cracks in wood, including cracks between wood ray parenchyma and longitudinal tracheids and between longitudinal tracheids. In addition, tearing of the cell wall along the microfibril angle and rupturing of the pit torus and pit margo on the pit membrane were observed in the wood using the HIMW treatment. The primary mode of cell wall destruction involved tearing from the junction of the S1/S2 interface and destruction in the S2 layer. Furthermore, HIMW treatment led to a slight change in the cell wall composition, namely cellulose, hemicellulose, and lignin. With the increase in MWED, hemicellulose degradation occurs first. The recrystallization of cellulose and the lignin content increases because the aromatic C=O groups change. The non-thermal effects of microwaves may affect the relative cellulose content of HIMW treatment samples, even though cellulose has greater thermal stability. These changes in chemical composition and structure consequently affected the crystallinity and crystal size of the cell wall. In particular, higher MWED correlated with increased relative crystallinity and crystal width. Cracks in wood and damage to cell walls can improve the drying rate and drying quality of wood. Moreover, in the functional modification impregnation of Chinese fir wood, suitable cracks can provide favorable channels for the penetration of impregnant chemicals so that the wood modifier can penetrate deeper and be distributed uniformly, thus improving the high efficiency and high value-added utilization of Chinese fir wood.

Author Contributions: Conceptualization, X.L. and X.G.; methodology, X.L.; software, X.F.; validation, X.G.; formal analysis, X.L.; data curation, X.L. and X.F.; writing—original draft preparation, X.L.; writing—review and editing, X.L. and Y.Z.; supervision, Y.Z. and S.Y.; funding acquisition, Y.Z. All authors have read and agreed to the published version of the manuscript.

Funding: This research was funded by the National Key R&D Program of China (2023YFD2201402), the National Project to Promote S&T Achievements in Forestry and Grassland (2020133146) and the National Natural Science Foundation of China (32101461). The APC was funded by the National Key R&D Program of China.

Data Availability Statement: The raw data supporting the conclusions of this article will be made available by the authors on request.

Conflicts of Interest: The authors declare no conflicts of interest.

References

- Ganguly, S.; Hom, S.K.; Tripathi, S.; Ghosh, S.; Kanyal, R.; Samani, A. Quantitative evaluation of microwave irradiation on short-rotation plantation wood species. *Maderas-Cienc. Tecnol.* **2021**, *23*, 1–14. [[CrossRef](#)]
- Yu, X.Y.; Wei, N.F.; Liu, Q.S.; Wu, Z.Y.; Fan, M.Z.; Zhao, W.G.; Zeng, Q.Z. Study on microwave pretreatment technology to improve the effect of shellac impregnation of fast-growing Chinese Fir. *J. Renew. Mater.* **2022**, *8*, 2041–2053. [[CrossRef](#)]
- Okon, K.E.; Lin, F.C.; Lin, X.; Chen, C.X.; Chen, Y.D.; Huang, B. Modification of Chinese fir (*Cunninghamia lanceolata* L.) wood by silicone oil heat treatment with micro-wave pretreatment. *Eur. J. Wood Wood Prod.* **2017**, *76*, 221–228. [[CrossRef](#)]
- Petty, J.A. Permeability and structure of the wood of Sitka spruce. *Proc. R. Lond.* **1970**, *175*, 149–166.
- Hansmann, C.; Gindl, W.; Wimmer, R.; Teischinger, A. Permeability of wood—A Review. *Wood Res.* **2002**, *47*, 1–16.
- Wardrop, A.B.; Davies, G.W. Morphological factors relating to the penetration of liquids into wood. *Holzforschung* **1961**, *15*, 129–141. [[CrossRef](#)]
- Bailey, P.J.; Preston, R.D. Some aspects of softwood permeability I. Structural studies with Douglas fir sapwood and heartwood. *Holzforschung* **1969**, *23*, 113–120. [[CrossRef](#)]
- Palin, M.A.; Petty, J.A. Permeability to water of the cell wall material of spruce heartwood. *Wood Sci. Technol.* **1981**, *15*, 161–166. [[CrossRef](#)]
- Torgovnikov, G.; Vinden, P. High-intensity microwave wood modification for increasing permeability. *For. Prod. J.* **2009**, *59*, 84–92.
- Torgovnikov, G.; Vinden, P. Microwave method for increasing the permeability of wood and its applications. *For. Prod. J.* **2010**, *60*, 303–311.
- Fan, Z.Q.; Peng, L.M.; Liu, M.H.; Feng, Y.; He, J.R.; Wu, S.Q. Analysis of influencing factors on sound absorption capacity in microwave-treated *Pinus radiata* wood. *Eur. J. Wood Wood Prod.* **2022**, *80*, 985–995. [[CrossRef](#)]
- Hermoso, E.; Vega, A. Effect of microwave treatment on the impregnability and mechanical properties of *Eucalyptus globulus* wood. *Maderas-Cienc. Tecnol.* **2016**, *18*, 55–64. [[CrossRef](#)]
- Zhang, J.X.; Luo, Y.F.; Liao, C.R.; Xiong, F.; Li, X.; Sun, L.L.; Li, X.J. Theoretical investigation of temperature distribution uniformity in wood during microwave drying in three-port feeding circular resonant cavity. *Dry. Technol.* **2017**, *35*, 409–416. [[CrossRef](#)]
- Weng, X. Study on the Influence Mechanism of Microwave Treatment on Drying Characteristics of Chinese Fir Wood. Ph.D. Thesis, Research Institute of Wood Industry, Chinese Academy of Forestry, Beijing, China, 2020.
- Mascarenhas, F.J.R.; Dias, A.M.P.G.; Christoforo, A.L. State of the art of microwave treatment of wood: Literature review. *Forests* **2021**, *12*, 745. [[CrossRef](#)]
- He, S.; Yu, H.; Wu, Z.X.; Chen, Y.H.; Fu, F. Effect of microwave treatment on liquid impregnate property of *Pinus Sylvestris*, L. var Lumber. *J. Microw.* **2016**, *32*, 90–96.
- Zhang, Y.L.; Jia, K.; Cai, L.P.; Shi, S.Q. Acceleration of moisture migration in Larch wood through microwave pre-treatments. *Dry. Technol.* **2013**, *31*, 666–671. [[CrossRef](#)]
- Xing, X.F.; Li, S.M.; Jin, J.W.; Lin, L.Y.; Zhou, Y.D.; Peng, L.M.; Fu, F. Improving gas permeability and characterizing the multi-scale pore size distribution of radiata pine (*Pinus radiata* D. Don) treated via high-intensity microwave. *Wood Sci. Technol.* **2023**, *57*, 1345–1367. [[CrossRef](#)]
- Terashima, N.; Fukushima, K.; He, L.F.; Takabe, K. Comprehensive model of the lignified plant cell wall. In *Forage Cell Wall Structure and Digestibility*; American Society of Agronomy, Inc.: Madison, WI, USA, 1993; pp. 247–270.
- Salmén, L.; Burgret, I. Cell wall features with regard to mechanical performance. A review COST Action E35 2004–2008: Wood machining-micromechanics and fracture. *Holzforschung* **2009**, *63*, 121–129. [[CrossRef](#)]
- Segal, L.; Creely, J.J.; Martin, A.E.; Conrad, C.M. An empirical method for estimating the degree of crystallinity of native cellulose using the X-ray diffractometer. *Text. Res. J.* **1962**, *29*, 786–794. [[CrossRef](#)]
- Nishiyama, Y.; Kuga, S.; Okano, T. Mechanism of mercerization revealed by X-ray diffraction. *J. Wood Sci.* **2000**, *46*, 452–457. [[CrossRef](#)]
- Saporiti, J. Effect of microwave treatment on oak compression strength. *Silva Lusit.* **2006**, *14*, 51–58.
- Kol, H.S.; Çayır, B. The effects of increasing preservative uptake by microwave pre-treatment on the microstructure and mechanical properties of Oriental spruce. *Wood Mater. Sci. Eng.* **2023**, *18*, 732–738. [[CrossRef](#)]
- Li, Z.; Zhan, T.; Eder, M.; Jiang, J.; Lyu, J.; Cao, J. Comparative studies on wood structure and microtensile properties between compression and opposite wood fibers of Chinese fir plantation. *J. Wood Sci.* **2021**, *67*, 12–18. [[CrossRef](#)]
- Muzamal, M. Structural Modifications in Spruce Wood during Steam Explosion Pretreatment. Ph.D. Thesis, Chalmers University of Technology, Gothenburg, Sweden, 2016.
- Tong, Y.P.; Zhao, G.J. Structure of bordered pit membrane of *Cunninghamia lanceolata* tracheid. *Sci. Silvae Sin.* **2007**, *43*, 151–153.
- Bao, F.C.; Lyu, J.X.; Zhao, Y.K. Effect of different positions of bordered pit torus in Yezo Spruce on its permeability. *Acta Bot. Sin.* **2001**, *43*, 119–126.
- Booker, R.E.; Sell, J. The nanostructure of the cell wall of softwoods and its functions in living tree. *Holz Roh Werkst.* **1998**, *56*, 1–8. [[CrossRef](#)]

30. Zhai, C.K.; Teng, N.; Pan, B.H.; Chen, J.; Liu, F.; Zhu, J.; Na, H.N. Revealing the importance of non-thermal effect to strengthen hydrolysis of cellulose by synchronous cooling assisted microwave driving. *Carbohydr. Polym.* **2018**, *197*, 414–421. [[CrossRef](#)] [[PubMed](#)]
31. Bichot, A.; Lerosty, M.; Radoiu, M.; Méchin, V.; Bernet, N.; Delgenès, J.-P.; García-Bernet, D. Decoupling thermal and non-thermal effects of the microwaves for lignocellulosic biomass pretreatment. *Energy Convers. Manag.* **2020**, *203*, 112220. [[CrossRef](#)]
32. Fackler, K.; Stevanic, J.S.; Ters, T.; Hinterstoisser, B.; Schwanninger, M.; Salmén, L. FTIR imaging microscopy to localise and characterise simultaneous and selective white-rot decay within spruce wood cells. *Holzforschung* **2011**, *65*, 411–420. [[CrossRef](#)]
33. Temiz, A.; Terziev, N.; Jacobsen, B.; Eikenes, M. Weathering, water absorption and durability of silicon, acetylated and heat-treated wood. *J. Appl. Polym. Sci.* **2006**, *102*, 4506–4513. [[CrossRef](#)]
34. Popescu, C.M.; Singurel, G.; Popescu, M.C.; Vasile, C.; Argyropoulos, D.S.; Willfor, S. Vibrational spectroscopy and X-ray diffraction methods to establish the differences between hardwood and softwood. *Carbohydr. Polym.* **2009**, *77*, 851–857. [[CrossRef](#)]
35. Lionetto, F.; Sole, R.D.; Cannoletta, D.; Vasapollo, G.; Maffezzoli, A. Monitoring wood degradation during weathering by cellulose crystallinity. *Materials* **2012**, *5*, 1910–1922. [[CrossRef](#)]
36. Huang, X.N.; Kocaefe, D.; Kocaefe, Y.; Boluk, Y.; Krause, C. Structural analysis of heat-treated birch (*Betula papyrifera*) surface during artificial weathering. *Appl. Surf. Sci.* **2013**, *264*, 117–127. [[CrossRef](#)]
37. Carrillo, F.; Colom, X.; Sunol, J.; Saurina, J. Structural FTIR analysis and thermal characterisation of lyocell and viscose-type fibres. *Eur. Polym. J.* **2004**, *40*, 2229–2234. [[CrossRef](#)]
38. Li, M.Y.; Cheng, S.C.; Li, D.; Wang, S.N.; Huang, A.M.; Sun, S.Q. Structural characterization of steam-heat treated *Tectona grandis* wood analyzed by FT-IR and 2D-IR correlation spectroscopy. *Chin. Chem. Lett.* **2015**, *26*, 221–225. [[CrossRef](#)]
39. Guo, J.; Song, K.L.; Salmén, L.; Yin, Y.F. Changes of wood cell walls in response to hygro-mechanical steam treatment. *Carbohydr. Polym.* **2015**, *115*, 207–214. [[CrossRef](#)]
40. Tarmian, A.; Mastouri, A. Changes in moisture exclusion efficiency and crystallinity of thermally modified wood with aging. *iFor.-Biogeosci. For.* **2019**, *12*, 92–97. [[CrossRef](#)]
41. Dwianto, W.; Tanaka, F.; Inoue, M.; Norimoto, M. Crystallinity changes of wood by heat or steam treatment. *Wood Res.* **1996**, *83*, 47–49.
42. Tribulová, T.; Kačík, F.; Evtuguin, D.V.; Čabalová, I.; Ďurkovič, J. The effects of transition metal sulfates on cellulose crystallinity during accelerated ageing of silver fir wood. *Cellulose* **2019**, *26*, 2625–2638. [[CrossRef](#)]
43. French, A.D. Idealized powder diffraction patterns for cellulose polymorphs. *Cellulose* **2014**, *21*, 885–896. [[CrossRef](#)]
44. Inagaki, T.; Siesler, H.W.; Mitsui, K.; Tsuchikawa, S. Difference of the crystal structure of cellulose in wood after hydrothermal and aging degradation: A NIR spectroscopy and XRD study. *Biomacromolecules* **2010**, *11*, 2300–2305. [[CrossRef](#)] [[PubMed](#)]
45. Rayirath, P.; Avramidis, S.; Mansfield, S.D. The effect of wood drying on crystallinity and microfibril angle in black spruce (*Picea mariana*). *J. Wood Chem. Technol.* **2008**, *28*, 167–179. [[CrossRef](#)]
46. Bhuiyan, M.T.R.; Hirai, N.; Sobue, N. Changes of crystallinity in wood cellulose by heat treatment under dried and moist conditions. *J. Wood Sci.* **2000**, *46*, 431–436. [[CrossRef](#)]
47. Guo, J.; Rennhofer, H.; Yin, Y.F.; Lichtenegger, H.C. The influence of thermo-hygro-mechanical treatment on the micro- and nanoscale architecture of wood cell walls using small- and wide-angle X-ray scattering. *Cellulose* **2016**, *23*, 2325–2340. [[CrossRef](#)]
48. Xing, D.; Li, J.; Wang, X.Z.; Wang, S.Q. In situ measurement of heat-treated wood cell wall at elevated temperature by nanoindentation. *Ind. Crops Prod.* **2016**, *87*, 142–149. [[CrossRef](#)]

Disclaimer/Publisher’s Note: The statements, opinions and data contained in all publications are solely those of the individual author(s) and contributor(s) and not of MDPI and/or the editor(s). MDPI and/or the editor(s) disclaim responsibility for any injury to people or property resulting from any ideas, methods, instructions or products referred to in the content.